



# Effect of Mn loading onto MnFeO nanocomposites for the CO<sub>2</sub> hydrogenation reaction

M. Al-Dossary<sup>a</sup>, Adel A. Ismail<sup>b,c,\*</sup>, J.L.G. Fierro<sup>a,\*\*</sup>, Houcine Bouzid<sup>b,d</sup>, S.A. Al-Sayari<sup>b,e</sup>

<sup>a</sup> Institute of Catalysis and Petroleum Chemistry, CSIC, Marie Curie 2, Cantoblanco, 28049, Madrid, Spain

<sup>b</sup> Promising Centre for Sensors and Electronic Devices (PCSED), Advanced Materials and Nano-Research Centre, Najran University, P.O. Box 1988, Najran 11001, Saudi Arabia

<sup>c</sup> Nanostructured Materials and Nanotechnology Division, Central Metallurgical Research and Development Institute (CMRDI), P.O. Box 87, Helwan, Cairo 11421, Egypt

<sup>d</sup> Laboratoire des Matériaux Ferroélectriques, Faculté des Sciences de Sfax, Route Soukra Km 3,5, BP 802, F-3018, Sfax, Tunisia

<sup>e</sup> College of Science and Arts-Sharoura, Najran University, Saudi Arabia

## ARTICLE INFO

### Article history:

Received 8 September 2014

Received in revised form 19 October 2014

Accepted 22 October 2014

Available online 1 November 2014

### Keywords:

Fischer–Tropsch synthesis (FTS)

CO<sub>2</sub> hydrogenation

Mn promotion

Fe-based catalysts

Fe-based FTS catalysts.

## ABSTRACT

This work describes the preparation of mesoporous xMnFe oxide ( $x = 0, 0.05, 0.1, 0.2, 0.3$  and  $0.5$  molar ratios) nanocomposites through a one-step sol–gel process in the presence of a triblock copolymer as a structure-directing agent. The prepared oxides were used as catalysts in the CO<sub>2</sub> hydrogenation via Fischer–Tropsch reactions for the production of valuable hydrocarbons. Among the catalysts, the 0.05MnFe catalyst performed best under the selected reaction conditions: a reaction temperature of 340 °C, overall pressure of 20 bar, reactant mixture of 23% CO<sub>2</sub>/69% H<sub>2</sub>/8% N<sub>2</sub> and flow rate of 20 mL min<sup>−1</sup>. This catalyst provided a much higher conversion of CO<sub>2</sub> to hydrocarbons (63.2% C<sub>2</sub>–C<sub>5</sub>, 3.9% to C<sub>6</sub>+ and 3.6% to oxygenates) and the lowest levels of CO and methane formation among the xMnFe series. Moreover, 0.05MnFe was the only catalyst with a mesoporous structure, and it had a substantially lower reduction temperature than did the other members of the series. The enhanced catalytic activity of the 0.05MnFe catalyst, which contains only a small amount of Mn, appears to result primarily from its high specific area and relatively easy reduction.

© 2014 Elsevier B.V. All rights reserved.

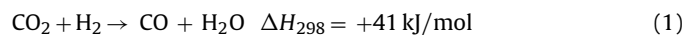
## 1. Introduction

Carbon dioxide emissions into the atmosphere from fossil fuel combustion are progressively increasing, with obvious effects on the climate. As fossil fuels will remain the world's primary energy source for decades to come, the stabilization of CO<sub>2</sub> levels in the atmosphere is one of the greatest challenges faced by the scientific community [1].

At present, recycling CO<sub>2</sub> to produce liquid renewable or sustainable hydrocarbons is one of the most interesting catalytic alternative options [2–8]. This conceptual approach offers the possibility of converting CO<sub>2</sub> into high-density transportation fuels compatible with our current storage and distribution network. A simple conversion route is the Fischer–Tropsch synthesis (FTS),

which provides clean synthetic fuels when starting with CO<sub>2</sub>-rich feeds [9–14].

FTS is a key technology employed over the last 90 years for the production of chemicals and clean transportation fuels from carbon sources alternative to unsustainable crude oil [15–17]. Alternative C-containing sources, such as biomass or coal, offer the possibility of producing H<sub>2</sub>-deficient or CO-rich syngas feeds. CO<sub>2</sub> hydrogenation comprises two reaction steps: the reverse water-gas shift (RWGS) reaction (Eq. (1)) and the Fischer–Tropsch (FT) reaction (Eq. (2)):



Compared with the traditional FT synthesis, twice as much hydrogen is needed in this two-step reaction, and more water is formed as a byproduct. Thermodynamically, as it is a slightly endothermic reaction, the conversion of CO<sub>2</sub> by RWGS is limited at the low temperatures used in the traditional FT reaction: at an H<sub>2</sub>/CO<sub>2</sub> ratio of 3 (stoichiometric ratio for CO<sub>2</sub> hydrogenation to  $-\text{CH}_2-$ ) only 13–23% of CO<sub>2</sub> is converted into CO at temperatures between 220 and 300 °C [18]. The exothermic FT reaction is

\* Corresponding author.

\*\* Corresponding author.

E-mail addresses: [adelali141@yahoo.com](mailto:adelali141@yahoo.com) (A.A. Ismail), [jlgfierro@icp.csic.es](mailto:jlgfierro@icp.csic.es) (J.L.G. Fierro).

not thermodynamically limited in the above temperature regime; thus, it is possible to achieve higher CO<sub>2</sub> conversion for the overall reaction because of the consecutive RWGS reaction, which forms CO.

Iron-based catalysts have been used for the hydrogenation of CO<sub>2</sub> to C<sub>2+</sub> hydrocarbons [19–24]. For these systems, it is generally accepted that, instead of the direct hydrogenation of CO<sub>2</sub>, the RWGS (Eq. (1)) proceeds over these catalysts, followed by the hydrogenation of CO to hydrocarbons (Eq. (2)) via the FT synthesis reaction. Fe-based catalysts can catalyze both the RWGS reaction [25] and the hydrogenation of CO and are thus expected to show good performance for the hydrogenation of CO<sub>2</sub>.

Compared to other metal catalysts employed for FTS, the iron-based catalysts provide higher conversion, selectivity to lower olefins and flexibility in terms of the process parameters [26–28]. However, catalysts containing Fe alone do not solve the problem of low selectivity to lower olefins, a general limitation of the FTS process. Manganese has been widely used as a promoter of FTS on iron catalysts, particularly for producing low olefins [29–32]. The individual effect of manganese promotion on supported or unsupported iron catalysts has also been the focus of much research effort [22,33–36].

Lohitharn and Goodwin [37] have indicated improved activity and/or selectivity upon the addition of transition metals to Fe-based FTS catalysts. It has been reported that incorporation of various transition metals other than Cu, such as Zr, Cr, Mo, Mn, Ta and V, greatly increased the catalyst activities for both CO hydrogenation and WGS to varying degrees [38]. Among the promoted iron-based catalysts, the Fe–Mn catalyst is of industrial interest and has been described extensively in recent years due to its higher olefin and middle distillate selectivity. For instance, Mn-promoted Fe catalysts with Mn loadings up to 15 wt% demonstrated greater light olefin (C<sub>2</sub>–C<sub>4</sub>) formation than their Mn-free counterpart [35,39–41]. In most studies, Mn–Fe oxides were prepared by the conventional co-precipitation of the hydroxides, which were then subjected to air calcination. Recently, Mn–Fe binary oxides have been synthesized by a template-free controlled thermal decomposition approach from single-phase Mn–Fe binary oxalate, which was prepared by precipitation from a Mn<sup>2+</sup>–Fe<sup>2+</sup> solution mixed with oxalic acid [42].

Mesoporous materials are considered promising for high-efficiency catalysts due to their high surface areas and large pore sizes. Therefore, our approach in the present work consisted of the preparation of mesoporous Mn–Fe nanocomposites through a simple one-step sol–gel process in the presence of a triblock copolymer as a structure-directing agent and their use for the CO<sub>2</sub> hydrogenation via FT synthesis for the production of higher hydrocarbons. This paper presents the results of our recent studies on the effects of manganese addition to MnFeO nanocomposites for the CO<sub>2</sub> hydrogenation reaction. The catalysts were investigated using different characterization techniques to establish the relationship between catalyst structure and performance.

## 2. Experimental

### 2.1. Materials

The block copolymer surfactant EO<sub>106</sub>–PO<sub>70</sub>EO<sub>106</sub> (F-127, EO = –CH<sub>2</sub>CH<sub>2</sub>O–, PO = –CH<sub>2</sub>(CH<sub>3</sub>)CHO–, MW 12,600 g/mol), iron(III) acetylacetonate (97%, Fe(C<sub>5</sub>H<sub>7</sub>O<sub>2</sub>)<sub>3</sub>), manganese(II) acetate tetrahydrate (99.99%, (CH<sub>3</sub>COO)<sub>2</sub>Mn·4H<sub>2</sub>O), HCl, C<sub>2</sub>H<sub>5</sub>OH and CH<sub>3</sub>COOH were purchased from Sigma–Aldrich.

### 2.2. Preparation of mesoporous Mn–Fe–O nanocomposites

Mesoporous Mn/Fe oxides were synthesized through a simple one-step sol–gel process in the presence of the F127 triblock

copolymer as a structure-directing agent. To homogeneously distribute manganese nanoparticles into the Fe<sub>2</sub>O<sub>3</sub> framework, we utilized a multicomponent assembly approach, wherein the surfactant, Mn and Fe<sub>2</sub>O<sub>3</sub> were assembled in a single-step process. First, 2.4 g of F127, 2.3 mL of CH<sub>3</sub>COOH and 0.74 mL of HCl were dissolved in 30 mL of ethanol, to which 2.28 g of Fe(C<sub>5</sub>H<sub>7</sub>O<sub>2</sub>)<sub>3</sub> was added under magnetic stirring for 60 min. Next, the appropriate amounts of (CH<sub>3</sub>COO)<sub>2</sub>Mn·4H<sub>2</sub>O were added to the F127–Fe(C<sub>5</sub>H<sub>7</sub>O<sub>2</sub>)<sub>3</sub>–CH<sub>3</sub>COOH mesophase to obtain manganese to iron molar ratios of 0, 0.05, 0.1, 0.2, 0.3 and 0.5. The mixture was continuously stirred for 2 h and then transferred into a Petri dish. The ethanol was evaporated at 40 °C and a relative humidity of 40% for 12 h, followed by the transfer of the sample into a 65 °C oven and aging for an additional 24 h. The as-made mesostructured hybrids were calcined at 450 °C in air for 4 h at a heating rate of 1 °C/min and a cooling rate of 2 °C/min to remove the surfactant and to obtain mesostructured manganese–iron oxides at different molar ratios (*x*). The samples are hereafter referred to as *x*MnFe, where *x* = 0, 0.05, 0.1, 0.2, 0.3 and 0.5.

### 2.3. Characterization techniques

#### 2.3.1. N<sub>2</sub> adsorption–desorption isotherms

Nitrogen adsorption–desorption isotherms were obtained with an Autosorb apparatus (Quantachrome Instruments) at liquid nitrogen temperature (–196 °C). Prior to analysis, the samples were subjected to vacuum (10<sup>–5</sup> mbar) at 200 °C for 22 h to ensure a clean surface. The surface areas were calculated by the Brunauer–Emmett–Teller (BET) method using the adsorption data within the *P*/*P*<sub>0</sub> range from 0.05 to 0.30. The pore volumes were measured at a relative pressure *P*/*P*<sub>0</sub> of 0.95. The pore size distribution was analyzed using the Barrett–Joyner–Halenda (BJH) model.

#### 2.3.2. High-resolution transmission electron microscopy (HRTEM)

Transmission electron microscopy (TEM) was conducted at 200 kV with a JEOL JEM-2100F-UHR field-emission instrument equipped with a Gatan GIF 2001 energy filter and a 1k CCD camera to record the EEL spectra. An energy-dispersive X-ray microanalysis (EDX) system was used to verify the semi-quantitative composition of the supported phases. The prepared catalysts were ultrasonically dispersed in acetone at room temperature and then spread over a holey carbon–copper microgrid. At least 10 representative images were recorded for each sample. To obtain statistically reliable information, the lengths of ca. 300 particles were measured.

#### 2.3.3. X-ray diffraction (XRD)

X-ray diffraction (XRD) data were acquired on a Bruker AXS D4 Endeavour X diffractometer using Cu Kα<sub>1/2</sub>, λ<sub>α1</sub> = 154.060 pm, λ<sub>α2</sub> = 154.439 pm radiation.

#### 2.3.4. Temperature-programmed reduction (TPR)

TPR experiments were performed on powder samples. The samples (30 mg) were loaded in a U-shaped tubular quartz reactor heated by an electrical furnace on-line with a Micromeritics TPD/TPR 2900 apparatus. The calcined precursors were reduced with 50 mL(STP)/min of a 10 vol.% H<sub>2</sub>/Ar reducing mixture. The temperature was progressively increased from room temperature to 900 °C at a linear programmed rate of 10 °C/min. A cold trap was placed at the outlet of the reactor to collect the water. H<sub>2</sub> was used as a reference gas, and the consumption of hydrogen was measured by comparison of the thermal conductivity difference between the reference and the product gas.

#### 2.3.5. X-ray photoelectron spectroscopy (XPS)

X-ray photoelectron spectra (XPS) were obtained using a VG Escalab 200R electron spectrometer equipped with a Mg Kα

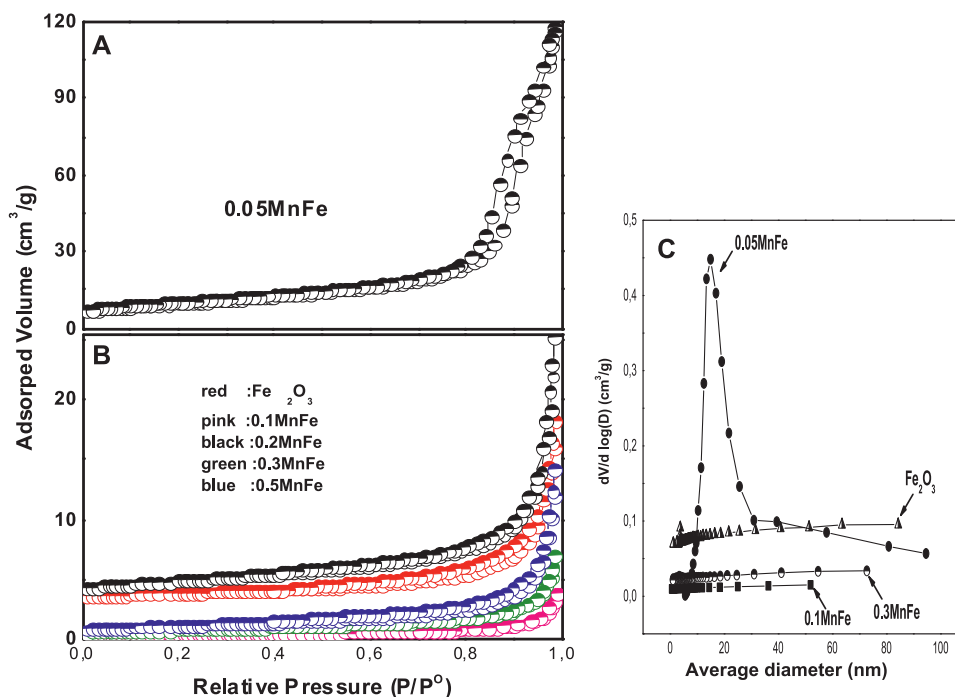


**Fig. 1.** Nitrogen adsorption–desorption isotherms of (A) 0.05MnFe, (B) Fe<sub>2</sub>O<sub>3</sub> and xMnFe samples with  $x = 0.05, 0.10, 0.20, 0.30$  and  $0.50$ , and (C) pore size distributions.

( $h\nu = 1253.6$  eV,  $1 \text{ eV} = 1.6302 \times 10^{-19}$  J) X-ray source powered at 100 W. The kinetic energies of photoelectrons were measured using a hemispherical electron analyzer working in constant-pass-energy mode. High-resolution spectra were recorded by scanning narrow kinetic energy windows (20–35 eV) at a pass energy of 50 eV. The linearity of the energy scale was calibrated against the Au 4f<sub>7/2</sub> (84.0 eV) and Cu 2p<sub>3/2</sub> (932.6 eV) photoemission lines by standard procedures. The background pressure in the analysis chamber was kept below  $2 \times 10^{-9}$  mbar during data acquisition. The XPS signals were recorded in increments of 0.07 eV with dwell times of 40 ms. The binding energies (BEs) were calibrated relative to adventitious carbon (C–C/C–H) using the C 1s peak at 284.8 eV. The peak intensities were estimated by calculating the integral of each peak after smoothing and subtraction of the Shirley background and fitting the experimental peak by a least-squares routine using Gaussian and Lorentzian lines (90 G/10 L). The atomic ratios were computed from the intensity ratios normalized by the atomic sensitivity factors [43].

#### 2.4. Catalytic activity

The catalysts were tested in the CO<sub>2</sub> hydrogenation reaction using a fixed-bed stainless-steel reactor. The reactor temperature was measured with a K-type thermocouple buried in the catalytic bed. All pipes after the reactor outlet were kept at 130 °C. The reaction system was equipped with a stainless-steel hot trap set at 120 °C to collect the heavier products. The flow rates were controlled using a Brooks 5850 TR series mass flow controller. To facilitate the heat transfer and to prevent hot spots resulting from the exothermal character of the reaction, the calcined catalysts (200 mg) were diluted with SiO<sub>2</sub> (ca. 1.8 g). First, the catalysts were activated *in situ* at 400 °C (heating rate of 10 °C min<sup>−1</sup>) for 5 h in pure hydrogen at atmospheric pressure. The reactor was then cooled to the reaction temperature (340 °C), after which the reactant gas mixture (23% CO<sub>2</sub>/69% H<sub>2</sub>/8% N<sub>2</sub>) was flowed through the activated catalyst at a flow rate of 20 mL min<sup>−1</sup> and the system was pressurized to 20 bar. This moment was considered the initial time of the reaction. Product analysis was performed on-line with a gas

**Table 1**

BET area, pore volume and pore size of mesoporous xMnFe samples.

Catalyst	BET area (m <sup>2</sup> /g)	Pore volume (cm <sup>3</sup> /g)	Pore size (nm)
Fe <sub>2</sub> O <sub>3</sub>	4.0	0.021	17.4
0.05MnFe	34.4	0.179	19.1
0.1MnFe	1.5	0.004	11.7
0.2MnFe	7.6	0.031	13.3
0.3MnFe	2.9	0.009	11.1
0.5MnFe	4.1	0.019	15.2

chromatograph (HP 6890 Plus). A Porapak Q (1/8" × 3 m)-packed column connected to a thermal conductivity detector was used to analyze the inorganic gases (H<sub>2</sub>, N<sub>2</sub>, CO, CO<sub>2</sub>) and water. Hydrocarbons and oxygenated compounds were analyzed with a DB-1 capillary column (60 m × 0.25 mm) connected to a flame ionization detector. The following temperature program was used: −50 °C for 10 min, a 10 °C min<sup>−1</sup> ramp up to 230 °C, and holding at this temperature for 20 min. N<sub>2</sub> was used as the internal standard for chromatographic analyses.

CO<sub>2</sub> conversion and selectivity to a given product are defined as follows:

$$X_{\text{CO}_2} = [(\text{moles CO}_2)_{\text{in}} - (\text{moles CO}_2)_{\text{out}}] / (\text{moles CO}_2)_{\text{in}} \times 100 \quad (3)$$

$$S_i(\%) = \text{moles of } i \text{ product} / [(\text{moles CO}_2)_{\text{in}} - (\text{moles CO}_2)_{\text{out}}] \times 100 \quad (4)$$

where  $X_{\text{CO}_2}$  is the conversion of CO<sub>2</sub>,  $S_i$  is the selectivity to product  $i$  and  $(\text{moles CO}_2)_{\text{in}}$  and  $(\text{moles CO}_2)_{\text{out}}$  are the number of moles of CO<sub>2</sub> at the reactor inlet and outlet, respectively.

### 3. Results

#### 3.1. Textural properties

The nitrogen adsorption–desorption isotherms and the BJH desorption pore size distribution plots of xMnFe are shown in Fig. 1, and the pore structure parameters are summarized in Table 1. Sample 0.05MnFe presented type IV isotherm patterns with an H3-type hysteresis loop, which are characteristic of mesoporous materials



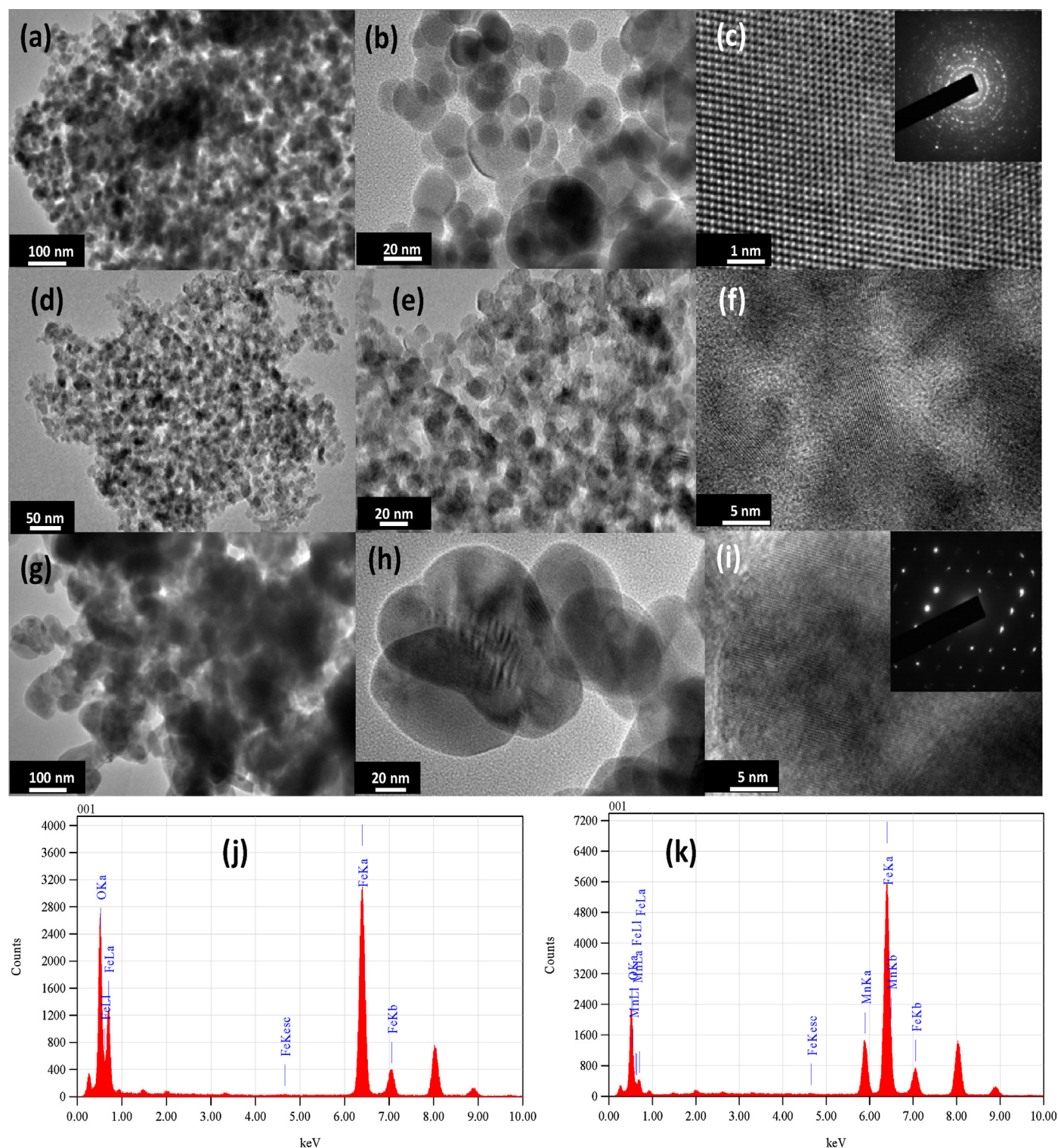


**Fig. 2.** TEM images of mesoporous  $\alpha$ -Fe<sub>2</sub>O<sub>3</sub> at low and high magnifications (a, b); HRTEM image of  $\alpha$ -Fe<sub>2</sub>O<sub>3</sub> and the insets show the SAED patterns for the  $\alpha$ -Fe<sub>2</sub>O<sub>3</sub> (c), 0.05MnFe nanocomposites at low and high magnifications (d, e); HRTEM image of 0.05MnFe nanocomposites (f), 0.3MnFe nanocomposites at low and high magnifications (g, h); HRTEM image of 0.3MnFe nanocomposites and the insets show the SAED patterns for the  $\alpha$ -Fe<sub>2</sub>O<sub>3</sub> (i). EDX spectra of  $\alpha$ -Fe<sub>2</sub>O<sub>3</sub> and 0.3 xMnFe (j, k).

with cylindrical pores formed in gallery regions [44]. This proves that the 0.05MnFe sample exhibits a mesoporous structure. For this sample, the onset of the hysteresis loop occurs at high relative pressure ( $P/P_0 = 0.62$ ), which corresponds to the beginning of capillary condensation in the pores. The upper closure point of the hysteresis loop, at which the pores are completely filled with liquid, is approximately  $P/P_0 = 0.99$ . In contrast, the other xMnFe

( $x = 0.1$ – $0.5$ ) samples show type IV isotherms with very thin H4 hysteresis loops, and the desorption branch of the isotherms of these samples extended to a lower pressure, suggesting a partial loss of structural organization and the formation of some narrower slit-shaped pores [45]. In addition, 0.05MnFe displays a relatively narrow pore size distribution with a maximum at 19.1 nm, however the pore size distribution for the other xMnFe samples are flat

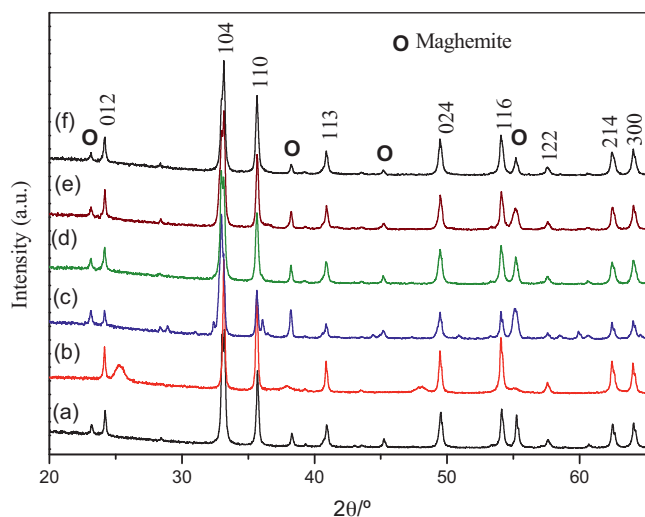


**Fig. 3.** (a) XRD of  $\alpha$ -Fe<sub>2</sub>O<sub>3</sub> and xMnFe nanocomposites at different molar ratios of 0.05 (b), 0.1 (c), 0.2 (d), 0.3 (e) and 0.5 (f) calcined at 450 °C for 4 h. Shifted for sake of clarity.

without any maximum (Fig. 1C). Both the BET areas and pore volumes are approximately one order of magnitude lower than those of the parent 0.05MnFe sample. It is also emphasized that the pore size of the 0.05MnFe sample is only slightly higher (19.1 nm) than that of the other members of the series (11.1–17.4 nm) (Table 1).

### 3.2. Morphology

The TEM images illustrate the morphology of the prepared mesoporous  $\alpha$ -Fe<sub>2</sub>O<sub>3</sub> and xMnFe nanocomposites at different molar ratios of 0.05 and 0.3Mn/Fe oxides (Fig. 2). The TEM images revealed that  $\alpha$ -Fe<sub>2</sub>O<sub>3</sub> is comprised of uniform granular crystals with a particle size of ~15 nm, and a worm-like disordered arrangement of the mesoporous  $\alpha$ -Fe<sub>2</sub>O<sub>3</sub> nanoparticles was obtained (Fig. 2a). At high magnification, the  $\alpha$ -Fe<sub>2</sub>O<sub>3</sub> nanoparticles are quite uniform in size and spherical in shape (Fig. 3b). Selected area electron diffraction (SAED) pattern (Fig. 2c, inset) further confirms that  $\alpha$ -Fe<sub>2</sub>O<sub>3</sub> nanocrystals are progressively formed. When Mn was added to  $\alpha$ -Fe<sub>2</sub>O<sub>3</sub> nanoparticles at a molar ratio of 0.05, TEM images at low and high magnification show worm-like pore shapes and consist of uniform nanoparticles with sizes of about 20 nm (Fig. 2d and e). With increasing Mn/Fe molar ratio to reach 0.3, TEM images show assembled agglomerations of nanoparticles with mesoporosity structure (Fig. 2g) as confirmed by the observation of solid irregular elliptical  $\alpha$ -Fe<sub>2</sub>O<sub>3</sub> nanoparticles (Fig. 2h) with an average diameter of ~40–50 nm (Fig. 2g and h). It is clearly seen that the particle sizes gradually increase with increasing Mn/Fe molar ratio. Energy-dispersive X-ray (EDX) spectra of the  $\alpha$ -Fe<sub>2</sub>O<sub>3</sub> and 0.3MnFe samples, with the latter being consistent with the Mn:Fe ratio used in the starting sol mixtures (Fig. 2j and k). The atomic planes of the  $\alpha$ -Fe<sub>2</sub>O<sub>3</sub> nanoparticles are separated by 3.7 Å, which agrees with the (012) crystallographic planes of  $\alpha$ -Fe<sub>2</sub>O<sub>3</sub> in the obtained composites (Fig. 2c, f and i).

### 3.3. Structural characteristics

Fig. 3 shows the X-ray diffraction patterns of the synthesized  $\alpha$ -Fe<sub>2</sub>O<sub>3</sub> and xMnFe nanocomposites at different molar ratios of  $x = 0.05, 0.1, 0.2, 0.3$  and  $0.5$ . The XRD patterns of the  $\alpha$ -Fe<sub>2</sub>O<sub>3</sub> and xMnFe nanocomposites correspond to a hexagonal structure of  $\alpha$ -Fe<sub>2</sub>O<sub>3</sub> with structural parameters of  $a = b = 5.038$  Å,  $c = 13.772$  Å, which are in good agreement with the recorded values of JCPDS File Card No. 33-0664. The obvious peaks at (012), (104) and (110)

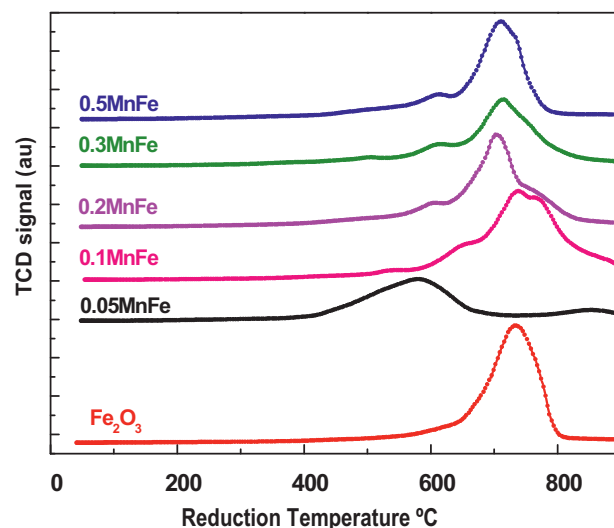


**Fig. 4.** TPR profiles of xMnFe nanocomposites at different Mn/Fe ratios.

**Table 2**

H<sub>2</sub> consumption during TPR experiments.

Catalyst	Theor. H <sub>2</sub> consumption (10 <sup>-4</sup> mol)	Exp. H <sub>2</sub> consumption (10 <sup>-4</sup> mol)
Fe <sub>2</sub> O <sub>3</sub>	2.82	1.7
0.05MnFe	2.74	0.94
0.1MnFe	2.66	1.09
0.2MnFe	2.48	1.59
0.3MnFe	2.28	1.32
0.5MnFe	1.82	1.53

suggest that the obtained  $\alpha$ -Fe<sub>2</sub>O<sub>3</sub> was well crystallized. The intensity of the (104) peak was higher than that of the (110) peak in all prepared samples, as shown in Fig. 3. It is clearly seen that the prepared samples can be mainly investigated as  $\alpha$ -Fe<sub>2</sub>O<sub>3</sub>, trace amount of maghemite and amorphous Mn oxides (Fig. 3). In addition, there is no trace maghemite at 0.05Mn/Fe sample. This is explained by at low Mn content, the prepared sample is almost magnetite and amorphous Mn oxides, however, maghemite phase appeared as a result of a trace phase transformation. No manganese oxide phases can be observed, suggesting that the manganese oxides are highly dispersed in the  $\alpha$ -Fe<sub>2</sub>O<sub>3</sub> network. However, XPS investigation (see below) confirmed that an amorphous MnO<sub>x</sub> phase covers the  $\alpha$ -Fe<sub>2</sub>O<sub>3</sub> nanoparticles.

### 3.4. Reducibility

The reducibility of the calcined xMnFe samples was investigated by TPR experiments, and the reduction profiles are displayed in Fig. 4. The reduction profile of the Mn-free Fe<sub>2</sub>O<sub>3</sub> sample shows only an asymmetric reduction peak with a maximum at approximately 730 °C. The TPR profiles of 0.2MnFe, 0.3MnFe and 0.5MnFe are quite similar to one another but somewhat different from that of Fe<sub>2</sub>O<sub>3</sub>: they show a very small H<sub>2</sub> consumption peak at approximately 610 °C, associated to reduction of Mn<sup>4+</sup> into Mn<sup>3+</sup>, and a very intense peak at approximately 710 °C, with a tail extending toward higher temperatures in the cases of 0.2MnFe and 0.5MnFe. However, the reduction profile of sample 0.05MnFe is quite different, being rather broad with a maximum at approximately 570 °C (150 °C below that observed for the Mn-free sample).

To quantify the extent of sample reduction up to a maximum reduction temperature of 900 °C, the TCD was calibrated, and the H<sub>2</sub> consumption was evaluated for all the xMnFe ( $x = 0$ – $0.5$ ) samples. Table 2 presents the H<sub>2</sub> consumption during reduction for

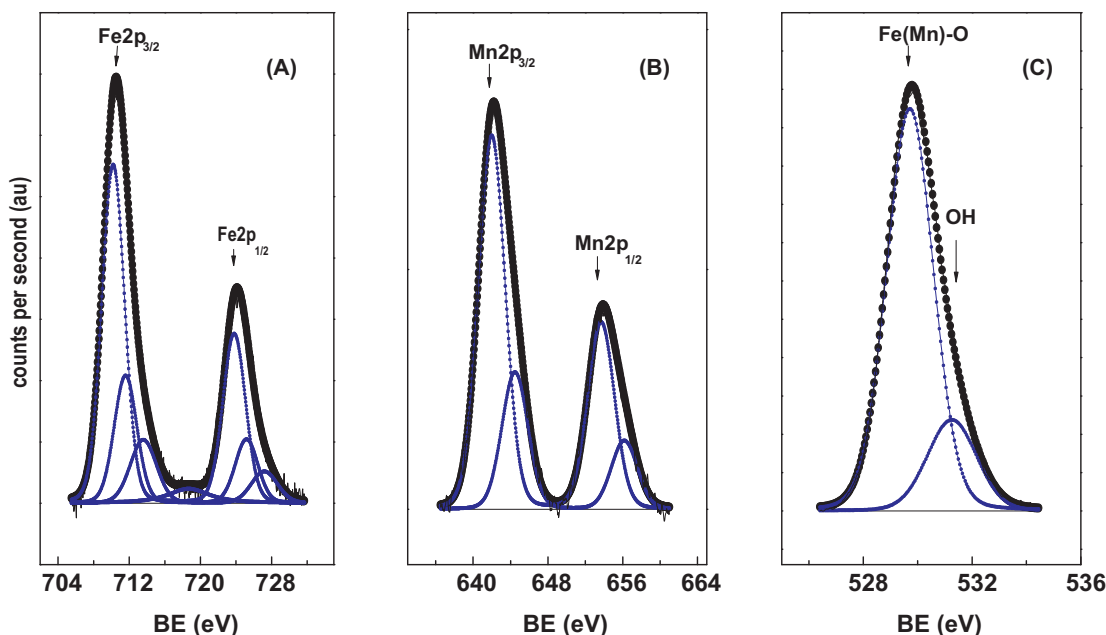


Fig. 5. Fe 2p (A), Mn 2p (B) and O 1s (C) core-level spectra of the representative 0.3MnFe sample.

all these samples. The maximum  $H_2$  consumption occurs for the  $Fe_2O_3$  sample ( $1.70 \times 10^{-4}$  mol), decreasing somewhat for samples 0.5MnFe ( $1.53 \times 10^{-4}$  mol), 0.3MnFe ( $1.32 \times 10^{-4}$  mol) and 0.2MnFe ( $1.59 \times 10^{-4}$  mol). Sample 0.05MnFe exhibited the lowest  $H_2$  consumption ( $0.94 \times 10^{-4}$  mol). To determine the reduction extent, the theoretical  $H_2$  consumption values were evaluated assuming that  $Fe_2O_3$  is completely reduced to Fe metal and that the initial manganese oxide is a spinel  $Mn_3O_4$  that is reduced to MnO according to the following equations:



The theoretical  $H_2$  consumptions expected for complete reduction according to these two equations are also compiled in Table 2. The comparison of the experimental  $H_2$  consumption with the theoretical values indicates that metallic Fe is not reached up to a maximum temperature of  $900^\circ C$  in any of the cases. This is clearly illustrated by the relatively low extent of reduction observed for the Mn-free sample ( $Fe_2O_3$ ), in which the reduction progressed only up to FeO and no metallic Fe was formed.

### 3.5. Surface analysis

Photoelectron spectroscopy was employed to reveal the chemical states and the relative concentrations of Mn and Fe on the surface of calcined xMnFe samples. For all the samples, high-resolution Fe 2p, Mn 2p and O 1s spectra were recorded and that of the representative 0.3MnFe sample is displayed in Fig. 5. Moreover, the corresponding binding energies of the Fe  $2p_{3/2}$ , Mn  $2p_{3/2}$  and O 1s core levels are summarized in Table 3.

The binding energy of the most intense Fe  $2p_{3/2}$  component of the Fe 2p doublet of the Mn-free sample ( $Fe_2O_3$ ) appears at 710.9 eV, which is typical of  $Fe^{3+}$  ions in an environment of oxide ions [46]. In addition, this sample and all other xMnFe samples show a small satellite line situated at approximately 718.9 eV, which is the fingerprint of  $Fe^{3+}$  ions. The data collected in Table 3 also indicate that the BE of the Fe  $2p_{3/2}$  peak of the other xMnFe samples is slightly lower (710.1–710.4 eV) than that of the Mn-free sample. For these xMnFe ( $x = 0.05$ – $0.50$ ) samples, the most intense Mn  $2p_{3/2}$

Table 3

Binding energies (eV) of the core levels of xMnFe samples.

Sample	Fe $2p_{3/2}$	Mn $2p_{3/2}$	O 1s	Mn/Fe at
$Fe_2O_3$	710.9	–	530.3 (79) 531.7 (21)	–
0.05MnFe	710.3 (70) 711.6 (30)	641.9	529.7 (77) 531.5 (23)	0.246
0.1MnFe	710.2 (74) 711.6 (26)	642.0	529.7 (81) 531.5 (19)	0.318
0.2MnFe	710.3 (57) 711.5 (43)	642.0	529.7 (80) 531.4 (19)	0.561
0.3MnFe	710.4 (68) 711.6 (32)	642.0	529.7 (84) 531.5 (16)	0.712
0.5MnFe	710.1 (45) 711.6 (55)	641.7	529.6 (83) 531.2 (17)	0.795

Values in parentheses are peak percentages.

peak of the doublet showed a similar BE value of 641.7–642.0 eV regardless of Mn content. Regarding the Fe 2p peaks, the Mn 2p lines show an asymmetric shape on the high-binding-energy side, which is associated with final state effects and therefore ignored. The BEs values of the Mn  $2p_{3/2}$  component (Table 3) suggest that manganese could be present in the oxidation state  $Mn^{3+}$ ; however, due to the close proximity of the BEs of  $Mn^{3+}$  and  $Mn^{4+}$ , precise assignment is not possible by considering only the energies recorded for the 2p core levels. Unambiguous assignment of the oxidation state of manganese oxides can be obtained by recording the Mn 3s level. Therefore, the multiplet Mn 3s core-level spectrum was also recorded for all Mn-containing xMnFe samples (spectra not shown here). This spectrum arises from the exchange interaction between the core-level electron (Mn 3s) and the unpaired electrons in the valence band level (Mn 3d) by photoelectron ejection [47]. The splitting energy ( $\Delta E$ ) of the Mn 3s level of the xMnFe samples is in the range 5.5–5.4 eV. According to [48,49], these values allow the calculation of the average oxidation state of Mn in the xMnFe samples as 2.6–2.7, which suggests that both  $Mn_2O_3$  and  $Mn_3O_4$  coexist on the surface region of the xMnFe catalysts.

The binding energies of the O 1s core-level spectra of xMnFe samples are also summarized in Table 3. The O 1s spectra consist of two O-containing bonds: metal oxide (Mn–O–Mn and Fe–O–Fe) at 529.3–530.3 eV and hydroxyl groups (Mn(Fe)–OH) at



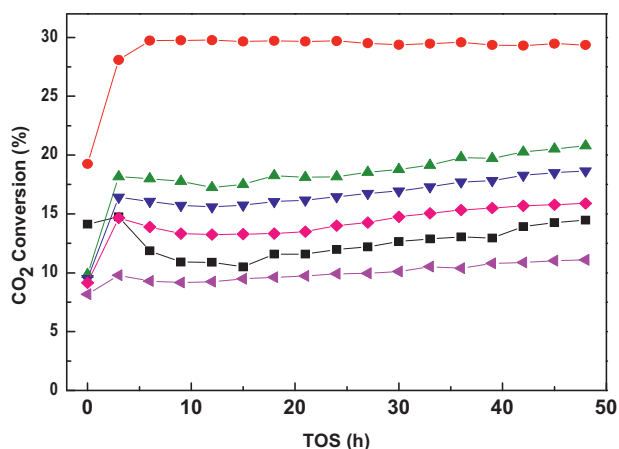


**Fig. 6.** Percentage of CO<sub>2</sub> conversion of different xMnFe catalysts as a function of time-on-stream (reaction conditions: 340 °C, 20 bar, CO<sub>2</sub>:H<sub>2</sub>:N<sub>2</sub> = 23:69:8 (molar)). (■) Fe<sub>2</sub>O<sub>3</sub>; (●) 0.05MnFe; (▲) 0.1MnFe; (▼) 0.2MnFe; (◆) 0.3MnFe; and (◄) 0.5MnFe.

531.5–531.7 eV [50]. No peak was detected at a binding energy somewhat above 533.0 eV, characteristic of adsorbed molecular water, indicating that the samples are completely dried. The hydroxyl content was rather low (16–23% of total oxygen). Quantification of surface species was also achieved using the XPS spectra. From the intensity ratios ( $I_{\text{Mn}}/I_{\text{Fe}}$ ) of the spectra, which were normalized by atomic sensitivity factors [43], atomic Mn/Fe ratios were computed, and the values are collected in Table 3 (last column). These values clearly indicate that Mn is strongly segregated toward the surface. Thus, the iron oxide nanoparticles are likely covered, at least to some extent, by an amorphous MnO<sub>x</sub> phase.

### 3.6. Catalytic performance

The CO<sub>2</sub> hydrogenation performances were investigated for xMnFe catalysts with different Mn loading to study the effect of Mn loading in the hydrogenation of CO<sub>2</sub> toward valuable products. Moreover, the CO<sub>2</sub> hydrogenation reaction was performed with the Mn-free (pure Fe<sub>2</sub>O<sub>3</sub>) catalyst for comparison. Fig. 6 illustrates the CO<sub>2</sub> conversion as a function of time on stream for the xMnFe catalysts. It is apparent that for all the catalysts tested under the selected reaction conditions (340 °C, 20 bar and a 23% CO<sub>2</sub>/69% H<sub>2</sub>/8% N<sub>2</sub> reactant mixture), a pseudo-stationary state is reached after approximately 5 h on stream. Nevertheless, the CO<sub>2</sub> conversion profiles differ by the value of  $x$ . The catalyst with the lowest Mn content (0.05MnFe) once activated maintains essentially constant CO<sub>2</sub> conversion over the time on stream of 48 h. However, the other catalysts, with atomic ratios  $x$  higher than 0.05, show a complex behavior in which the CO<sub>2</sub> conversion drops slightly at times on stream in the range 5–15 h and then progressively increases without reaching a plateau by the end of the duration test (48 h). These observations suggest that catalyst activation involves three different processes: (i) a fast initial activation; (ii) a subsequent slight drop in the FTS rate, due very likely to slower FTS rate as compared to the carbide formation rate; and (iii) slow increase of the FTS rate as a consequence of the higher concentration of active C\* species available on the surface when carbide formation level is high. The activity profiles also indicate that a small amount of Mn (as used in the 0.05MnFe catalyst) drastically improves the performance (30% CO<sub>2</sub> conversion) with respect to the Fe<sub>2</sub>O<sub>3</sub> catalyst (ca. 12% CO<sub>2</sub> conversion). However, a further increase in the Mn/Fe molar ratio (0.2MnFe and 0.5MnFe catalysts) inhibited CO<sub>2</sub> hydrogenation activity. This is illustrated by the CO<sub>2</sub> conversions of 16.5 and 10% achieved by the 0.2MnFe and 0.5MnFe catalysts, respectively.

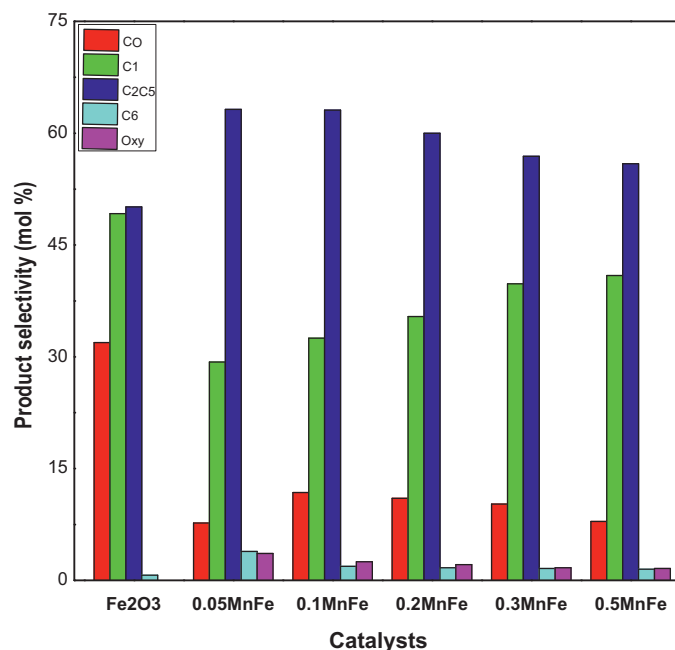


**Fig. 7.** CO, hydrocarbon and oxygenate selectivity for all the xMnFe catalysts (reaction conditions as in Fig. 6).

**Table 4**

Product selectivity and olefin/paraffin ratio of the xMnFe catalysts.

Catalyst	Fe <sub>2</sub> O <sub>3</sub>	0.05MnFe	0.1MnFe	0.2MnFe	0.3MnFe	0.5MnFe
CO	31.9	7.7	11.8	11	10.2	7.92
C <sub>1</sub>	49.2	29.3	32.5	35.4	39.8	40.9
C <sub>2</sub> –C <sub>5</sub>	50.1	63.2	63.1	60	56.9	55.9
C <sub>6</sub> +	0.7	3.9	1.9	1.7	1.6	1.5
Oxy	0	3.6	2.5	2.1	1.7	1.6
O/P	0.31	0.37	0.40	0.49	0.7	0.79

Reaction conditions as in Fig. 6. Carbon balance was in all cases between 93 and 99%.

It is worth mentioning that the CO<sub>2</sub> conversion obtained using the 0.5MnFe catalyst is lower than that using the Mn-free (Fe<sub>2</sub>O<sub>3</sub>) catalyst. Based on these results on the effect of the Mn/Fe molar ratio in the range  $x = 0.05$ – $0.50$ , it is evident that only a very small amount of Mn (as used in the 0.05MnFe catalyst) strongly promoted the CO<sub>2</sub> hydrogenation toward hydrocarbon formation and led to the optimum activity. The drop in catalytic activity with increasing Mn content in the catalyst formulation could be due to partial coverage of the active sites, i.e., Fe carbide phases, by the amorphous Mn oxide/carbide phases, which in turn prevent the reactant from making contact with the active centers.

Fig. 7 shows the CO and hydrocarbon selectivities including oxygenated components, and Table 4 compiles the product selectivities, including the olefins/paraffins ratio. It is worth mentioning that the hydrocarbon selectivities (HC) are reported here on a CO-free basis. Compared to the Mn-free (Fe<sub>2</sub>O<sub>3</sub>) catalyst, the 0.05MnFe catalyst inhibited CH<sub>4</sub> formation to some extent. For the 0.05MnFe catalyst, the CO selectivity was approximately 8%, which is much lower than the value of 32% recorded for the Fe<sub>2</sub>O<sub>3</sub> catalyst.

Reaction conditions as in Fig. 6. Carbon balance was in all cases between 93 and 99%. Moreover, this catalyst promoted the formation of valuable hydrocarbons, such as C<sub>2</sub>–C<sub>5</sub>, higher-molecular-weight hydrocarbons (C<sub>6</sub>+) and oxygenated products. From the data compiled in Table 4, it is clear that the Mn loadings higher than  $x = 0.05$  are detrimental to the production of useful products. In those catalysts, the selectivity to CH<sub>4</sub> increases at the expense of valuable product formation, such as C<sub>2</sub>–C<sub>5</sub>, C<sub>6</sub>+

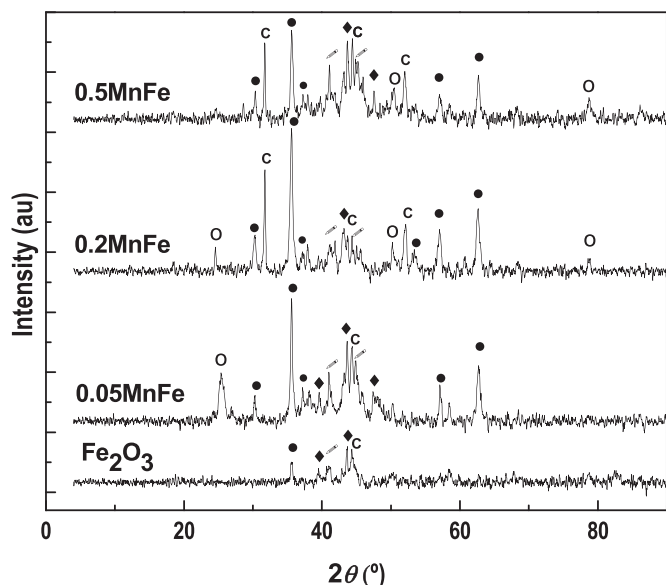


**Fig. 8.** XRD patterns for the used catalysts with different manganese contents. Reaction conditions: 340 °C, 20 bar, CO<sub>2</sub>:H<sub>2</sub>:N<sub>2</sub> = 23:69:8 (molar) for 48 h. (●) magnetite; (◆) carbide; (■) magnetite and carbide; (c) carbon; (○) unknown phase.

oxygenates. The only advantage of the xMnFe ( $x > 0.05$ ) catalysts is their higher effectiveness for increasing the olefin/paraffin ratio.

Chain growth probability ( $\alpha$ ) was calculated (Fig. S1) and its values of some representative catalysts are summarized in Table S1. The lowest  $\alpha$  value (0.30) was recorded for the Mn-free ( $x = 0$ ) catalyst, then increased for 0.05MnFe (0.43) and finally decreased for 0.2MnFe (0.35) and 0.5MnFe (0.33). It has been reported that since CO<sub>2</sub> hydrogenation follows a reaction mechanism similar to that of CO hydrogenation (with a previous CO<sub>2</sub> shift reaction) [53,54], the product distribution for both reactions should be very similar when using the same catalyst and reaction conditions. The relatively low values of chain growth probability measured in this work can be explained in terms of the low residence time employed in the reaction tests.

### 3.6.1. Structural and surface characteristics of used catalysts

The nature of surface species in Fe-based catalysts changes dramatically when exposed to the reaction employed in the CO<sub>2</sub> hydrogenation reaction. Characterization of both surface and bulk structures by XPS and XRD techniques demonstrated that  $\alpha$ -Fe<sub>2</sub>O<sub>3</sub> is the principal crystalline phase present in xMnFe catalyst precursors (cf. Figs. 3 and 5). However, this  $\alpha$ -Fe<sub>2</sub>O<sub>3</sub> phase disappeared completely and new ones were developed in the xMnFe catalysts exposed to the reactant mixture (23% CO<sub>2</sub>/69% H<sub>2</sub>/8% N<sub>2</sub>) at 300 °C, 20 bar overall pressure for a time on stream of 48 h.

The XRD patterns of some representative used xMnFe catalysts are displayed in Fig. 8. These patterns show diffraction lines at 39.3°, 40.9°, 43.9°, 44.9° and 47.2° assigned to iron carbide (Hägg carbide,  $\chi$ -Fe<sub>5</sub>C<sub>2</sub>) [51] and other diffractions at 30.1°, 35.5°, 37.1°, 57° and 62.6° typical of magnetite (Fe<sub>3</sub>O<sub>4</sub>) [53]. It is known that magnetite is responsible for the RWGS reaction, whereas iron carbide is highly catalytically active for FTS [53]. In addition, diffraction lines belonging to graphitic carbon together with lines of an unidentified species are clearly distinguished. It is also observed in Fig. 8 that the number and intensity of the diffraction lines increase with increasing value of  $x$ . This indicates that the extent of formation of iron carbide(s) and phases depend of the Mn content of the catalysts. As the diffraction lines of crystalline  $\chi$ -Fe<sub>5</sub>C<sub>2</sub> were almost absent in the Mn-free (Fe<sub>2</sub>O<sub>3</sub>) catalysts, it is suggested that

manganese oxide accelerates the generation of the  $\chi$ -Fe<sub>5</sub>C<sub>2</sub> phase in the catalysts maintained for 48 h on stream [54].

The nature of surface species of used xMnFe catalysts was investigated by XPS. The binding energies of core levels and surface atomic ratios are summarized in Table S2. The Fe 2p spectra of used xMnFe catalysts were satisfactorily fitted to two components: a major one at a binding energy of 710.5–710.7 eV associated to Fe<sub>3</sub>O<sub>4</sub> and a minor one at 708.1–708.3 eV which is characteristic of the Hägg carbide ( $\chi$ -Fe<sub>5</sub>C<sub>2</sub>). The Fe 2p spectra of some representative catalysts are displayed in Fig. 9A. These spectra show clearly that the intensity of the Fe 2p doublet of carbide species is maximum for the Mn-free sample and then decreases progressively upon increasing  $x$ . Moreover, the C 1s core-level spectra of used xMnFe catalysts exhibited three components (Fig. 9B) at binding energies of: 284.8 eV due to sp<sup>3</sup> C from contamination, 283.1–283.4 eV associated to carbidic carbon and at ca. 281.3 eV originated by graphitic carbon [55,56].

Atomic C/Fe ratios were also computed from the C 1s and Fe 2p core-level spectra and results are also compiled in Table S2. In this calculation, only carbidic iron and carbidic carbon components were selected for such calculations. It can be noted that the average C/Fe ratio of carbidic species is 0.49, slightly higher than the nominal value expected for the Hägg carbide ( $\chi$ -Fe<sub>5</sub>C<sub>2</sub>) whose nominal value is 0.40. This result suggests that the most abundant iron carbide phase in used xMnFe catalyst is the  $\chi$ -Fe<sub>5</sub>C<sub>2</sub> phase. Table S2 also summarizes the Mn/Fe atomic ratios of used catalyst. The values of these ratios are higher than that reported in Table 3 for the fresh (oxidic) samples, suggesting than additional segregation of manganese oxides toward the surface occurs during the carbidation of the catalysts during on stream operation.

## 4. Discussion

### 4.1. Catalysts structure

As prepared, the xMnFe catalysts consist of a crystalline  $\alpha$ -Fe<sub>2</sub>O<sub>3</sub> phase and amorphous Mn oxides. The EDX spectra indicated the presence of Fe and Mn elements and confirmed that the final xMnFe nanocomposite structures are consistent with the nominal Mn/Fe ratios. Notwithstanding, the highly sensitive XPS technique demonstrated that all the catalyst surfaces became Mn-enriched. There is no contradiction between the information provided by the EDX and XPS techniques, but the latter is surface-sensitive and thus obtains structural information from a low number of atomic layers beneath the surface layer, typically approximately 3 nm, whereas the X-rays recorded in the EDX technique originate from depth of a few micrometers. Therefore, Mn enrichment is only confined to a few atomic layers (surface and sub-surface layers).

Perhaps the most relevant differences among the xMnFe catalyst series are the much higher BET area and easier reduction of the 0.05MnFe catalyst. The lower BET area for the other xMnFe catalysts with  $x > 0.05$  suggests that the template approach employed here is not appropriate for high Mn loading. It is emphasized that the ease with which the 0.05MnFe catalyst is reduced compared to the other catalyst members of the series is essential, as it could favor the carbidation of Fe oxide phases. As will be shown in the following section, the 0.05MnFe catalyst is fully activated during the first 5 h on stream, and its performance remains stable throughout the 48-h duration of the test.

### 4.2. Effect of Mn on performance

It is known that the formation of hydrocarbons from CO<sub>2</sub> takes place via the two-step mechanism of the RWGS reaction and FT reaction [57]. Over Fe catalysts, CO is an important reaction



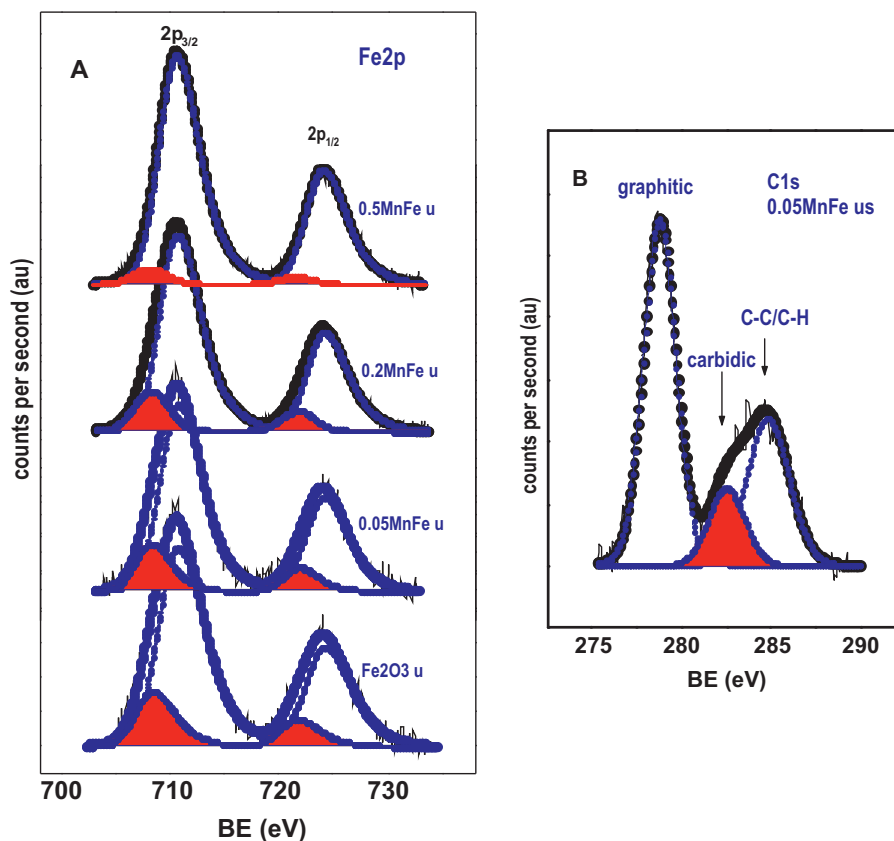


**Fig. 9.** (A) Fe 2p core-level spectra of some used xMnFe catalysts. The minor Fe 2p doublet in red color refers to iron carbide species. (B) C 1s spectrum of the representative 0.05MnFe used catalyst. The different carbon species are indicated by arrows.

intermediate in the conversion of CO<sub>2</sub> to higher hydrocarbons over Fe-based catalysts [58]. However, the unpromoted Fe-based catalysts are not selective for the desired FT products. Manganese is one of the promoters of Fe catalysts investigated in some detail because it influences the selectivity to higher hydrocarbons. From a mechanistic viewpoint, manganese not only improves the reducibility of iron oxide, but also modifies the distribution of iron species and catalyst basicity [22,41]. The data shown in Fig. 7 and Table 3 indicate unambiguously that the positive effect of Mn is only valid in a limited concentration range. Manganese-to-iron ratios higher than 0.05 appear detrimental for the production of useful C<sub>2</sub>–C<sub>5</sub>, C<sub>6</sub>+ and oxygenated products due to increasing CH<sub>4</sub> formation (cf. Table 3) and decreasing CO<sub>2</sub> conversion. A possible reason for this effect may be that high manganese loadings and particularly the highly segregated manganese oxide on the surface (cf. Table 3 and S2) limit the accessibility of reactants to the active Fe phase. Thus, to maintain the performance of the Fe active phases, it is essential to avoid or minimize the coverage/blockage of such phases by the amorphous MnO<sub>x</sub> phases.

In the course of CO<sub>2</sub> hydrogenation, it was demonstrated that CO formation is the essential step for producing C<sub>2</sub>+ hydrocarbons with high conversion and selectivity. The higher performance of the 0.05MnFe catalyst for the RWGS reaction would certainly contribute to the increase in the C<sub>2</sub>+ hydrocarbon formation from CO<sub>2</sub> under 20 bar of overall pressure. The selectivity to CH<sub>4</sub> in hydrocarbons decreases greatly for the 0.05MnFe catalyst, while the selectivity to C<sub>2</sub>–C<sub>5</sub> hydrocarbons follows an opposite trend. This could be associated to the preference for the adsorption of CO<sub>2</sub> rather than H<sub>2</sub> on this catalyst; however, H<sub>2</sub> is expected to diffuse better than CO<sub>2</sub> toward the active phase when higher amounts of Mn are incorporated ( $x > 0.05$ ). For these catalysts, the relative low CO<sub>2</sub>/H<sub>2</sub> ratio on the active sites would most likely favor methane

formation. It is reported that olefins are formed as a primary product over paraffins and undergo hydrogenation in the secondary steps [59]. Although it is expected that the CO<sub>2</sub>/H<sub>2</sub> ratio reaching the active sites is relatively high, the overall H<sub>2</sub> concentration should be lower than for its 0.05MnFe counterpart, a favorable olefin formation condition. This tendency was observed in the finding of an improved selectivity toward olefins in the C<sub>2</sub>–C<sub>5</sub> fraction for high values of  $x$ .

#### 4.3. Insights into the nature of the active phase

It is generally accepted that iron carbides, rather than metallic iron or iron oxides, are the active species in FT synthesis reactions [60–63]. Under FTS reaction temperatures as high as the one employed in this work (340 °C), many reports agreed that the active phase is  $\chi$ -Fe<sub>5</sub>C<sub>2</sub> carbide, whereas  $\theta$ -Fe<sub>3</sub>C carbide is a deactivation or spectator phase [64]. According to a volcano plot for metal–CO bond strength versus FT activity for Fe (and Co) catalysts, increasing the carbon content in iron carbide will weaken the Fe–CO bonding and therefore enhance catalyst activity.

The results reported here allow to firm conclusions to be drawn on the type of iron carbide developed on catalyst surface. The Fe 2p spectra of representative catalysts used in CO<sub>2</sub> hydrogenation for 48 h on stream (Fig. 9A) unambiguously demonstrate that the Hägg carbide ( $\chi$ -Fe<sub>5</sub>C<sub>2</sub>) is the major carbide phase developed on the catalyst surface. However, very likely other iron carbide phases may also be present as one would infer from the plethora of diffraction lines observed in used catalysts, and especially for the catalysts with  $x > 0.05$ . Moreover, other iron carbides different from  $\chi$ -Fe<sub>5</sub>C<sub>2</sub> are expected to display very similar binding energies of the most intense Fe 2p<sub>3/2</sub> line of the Fe 2p doublet. The data displayed in Fig. 6 clearly indicate that the catalyst 0.05MnFe became carbided

in approximately 5 h using the  $\text{H}_2/\text{CO}_2/\text{N}_2$  mixture under 20 bar overall pressure and maintained stationary-state conversion for the duration of the test (48 h on stream). In contrast, the other xMnFe catalysts, including  $\text{Fe}_2\text{O}_3$ , were initially carbided over the first 5 h but were then slowly deactivated for approximately 10 additional hours, very likely by the accumulation of carbon. At longer times, another slow carbidation process took place. It is also noted that no stationary state could be reached during the testing period (48 h). As noted above, with the exception of 0.05MnFe catalyst, all catalysts displayed very low specific areas, which might impede carbon diffusion and therefore make carbidation an extremely slow process.

## 5. Conclusions

Manganese-iron oxide (xMnFe,  $x=0\text{--}0.5$ ) catalysts were prepared by a template approach and then tested in the hydrogenation of  $\text{CO}_2$  into hydrocarbons/oxygenate products. The results obtained lead to the following conclusions. (i) Only the 0.05MnFe catalysts exhibited a mesoporous structure and moderately high BET area. (ii) Surface analysis by XPS showed a Mn-enriched surface (in a ca. 3-nm region). (iii) The 0.05MnFe catalyst was found to be reduced at much lower temperatures (maximum at  $570^\circ\text{C}$ ) than the other members of the series (maximum at approximately  $730^\circ\text{C}$ ) and was also easily carbided during the activation step. (iv) Under fixed reaction conditions (20 bar,  $340^\circ\text{C}$ ,  $\text{CO}_2:\text{H}_2:\text{N}_2=23:69:8$  (molar)), the Mn loading was found to exert a strong influence on  $\text{CO}_2$  conversion and selectivity to different products. (v) The 0.05MnFe catalyst displayed the best performance with reduced CO and  $\text{CH}_4$  formation and improved selectivity to  $\text{C}_2\text{--C}_5$  and  $\text{C}_6+$  hydrocarbons as well as the formation of some oxygenates.

## Acknowledgment

This research was supported by Najran University, Najran, the Kingdom of Saudi Arabia.

## Appendix A. Supplementary data

Supplementary data associated with this article can be found, in the online version, at <http://dx.doi.org/10.1016/j.apcatb.2014.10.064>.

## References

- [1] Z. Jiang, T. Xiao, V.L. Kuznetsov, P.P. Edwards, *Philosophical Transactions of the Royal Society A* 368 (2012) 3343.
- [2] M. Aresta, A. Dibenedetto, *Dalton Transactions* 28 (2007) 2975.
- [3] G. Centi, S. Perathoner, *Catalysis Today* 148 (2009) 191.
- [4] G.A. Olah, *Angewandte Chemie-International Edition* 44 (2005) 2636.
- [5] Q. Wang, J. Luo, Z. Zhong, A. Borgna, *Energy and Environmental Science* 4 (2011) 42.
- [6] A.J. Hunt, E.H.K. Sin, R. Marriott, J.H. Clark, *ChemSusChem* 3 (2010) 306.
- [7] A. Goepfert, M. Czaun, G.K.S. Prakash, G.A. Olah, *Energy Environmental Science* 5 (2012) 7833.
- [8] R. Ladera, F.J. Perez-Aonso, J.M. Gonzalez-Carballo, M. Ojeda, S. Rojas, J.L.G. Fierro, *Applied Catalysis B: Environmental* 142–143 (2013) 241.
- [9] L.M. Chew, H. Ruland, H.J. Schulte, W. Xia, M. Muhler, *J. Chem. Sci.* 126(2) (2014) 481.
- [10] X.Y. Quek, Y. Guan, R.A. van Santen, E.J.M. Hensen, *ChemCatChem* 3 (2011) 1735.
- [11] Q. Zhang, J. Kang, Y. Wang, *ChemCatChem* 2 (2010) 1030.
- [12] M. Feyzi, A. Hassankhami, *Journal of Natural Chemistry* 20 (2011) 677.
- [13] W. Wang, S.P. Wang, X.B. Ma, J.L. Gong, *Chem. Soc. Rev.* 40 (2011) 3703.
- [14] Z. You, W. Deng, Q. Zhang, Y. Wang, *Chinese Journal of Catalysis* 34 (2013) 956.
- [15] A.Y. Khodakov, W. Chu, P. Fongarland, *Chemical Review* 107 (2007) 1692.
- [16] H.M.T. Galvis, J.H. Bitter, C.B. Khare, M. Ruitenbeek, A.I. Dugulan, K.P. de Jong, *Science* 335 (2012) 835.
- [17] V.R. Calderone, N.R. Shiju, D. Curulla-Ferré, S. Chambrey, A. Khodakov, A. Rose, J. Thiessen, A. Jess, G. Rothenberg, *Angewandte Chemie-International Edition* 52 (2013) 4397.
- [18] U. Rodemerck, M. Holena, E. Wagner, Q. Smejkal, A. Barkschat, M. Baerns, *ChemCatChem* 5 (2013) 1948.
- [19] S.S. Nam, H. Kim, G. Kishan, M.J. Choi, K.W. Lee, *Applied Catalysis A: General* 179 (1999) 155.
- [20] M.L. Cubeiro, H. Morales, M.R. Goldwasser, M.J. Pérez-Zurita, F. González-Jiménez, G. Urbina, *Applied Catalysis A: General* 189 (1999) 87.
- [21] T. Riedel, H. Schulz, G. Schaub, K.W. Jun, J.S. Hwang, K.W. Lee, *Topics in Catalysis* 26 (2003) 41.
- [22] T. Herranz, S. Rojas, F.J. Pérez-Alonso, M. Ojeda, P. Terreros, J.L.G. Fierro, *Applied Catalysis A: General* 311 (2006) 66.
- [23] R.W. Dörner, D.R. Hardy, F.W. Williams, B.H. Davis, H.D. Willauer, *Energy and Fuels* 23 (2009) 4190–4195.
- [24] R.W. Dörner, D.R. Hardy, F.W. Williams, H.D. Willauer, *Applied Catalysis A: General* 373 (2010) 112–121.
- [25] Q. Zhang, J. Kang, Y. Wang, *ChemCatChem* 2 (2010) 1030.
- [26] C. Pirola, M. Scavini, F. Galli, S. Vitali, A. Comazzi, F. Manenti, P. Ghigna, *Fuel* 132 (2014) 62–70.
- [27] N.G. Hamilton, R. Warringham, I.P. Silverwood, J. Kapitán, L. Hecht, P.B. Webb, R.P. Tooez, W. Zhou, C.D. Frost, S.F. Parker, D. Lennon, *Journal of Catalysis* 312 (2014) 221.
- [28] J. Lu, L. Yang, B. Xu, Q. Wu, D. Zhang, S. Yuan, Y. Zhai, X. Wang, Y. Fan, Z. Hu, *ACS Catalysis* 4 (2) (2014) 613.
- [29] B.H. Davis, *Catalysis Today* 84 (2003) 83.
- [30] S. Soled, E. Iglesia, *Catalysis Letters* 7 (1990) 271.
- [31] Y. Jin, A.K. Dartye, *Journal of Catalysis* 196 (2000) 8.
- [32] A.P. Steynberg, M.E. Dry (Eds.), *Studies in Surface Science and Catalysis*, No. 152, Elsevier, Amsterdam, 2004.
- [33] G.P. van der Laan, A.A.C.M. Beenackers, *Catalysis Reviews-Science and Engineering* 41 (3–4) (1999) 255.
- [34] Y. Liu, B.-T. Teng, X.-H. Guo, Y. Li, J. Chang, L. Tian, X. Hao, Y. Wang, H.W. Xiang, Y.Y. Xu, Y. Wang, *Journal of Molecular Catalysis A: Chemical* 272 (1–2) (2007) 182.
- [35] T. Li, Y. Yang, C. Zhang, X. An, H. Wan, Z. Tao, H. Xiang, Y. Li, F. Yi, B. Xu, *Fuel* 86 (7–8) (2007) 921.
- [36] Y. Yang, H.-W. Xiang, L. Tian, H. Wang, C.-H. Zhang, Z.-C. Tao, Y.-Y. Xu, B. Zhong, Y.-W. Li, *Applied Catalysis A: General* 284 (1–2) (2005) 105.
- [37] N. Lohitharn, J.G. Goodwin, *Journal of Catalysis* 260 (2008) 7.
- [38] R.W. Dörner, H.D. Willauer, D.R. Hardy, F.W. Williams, *Report NRL/MR/6180-09-9200*, 2009.
- [39] R. Malessa, M. Baerns, *Industrial Engineering Chemistry Research* 27 (1988) 279.
- [40] L. Bai, H.W. Xiang, Y.W. Li, Y.Z. Han, B. Zhong, *Fuel* 81 (2002) 1577.
- [41] N. Lohitharn, J.G. Goodwin Jr., E. Lotero, *Journal of Catalysis* 255 (2008) 104.
- [42] Z. Shu, Y. Chen, W. Huang, X. Cui, L. Zhang, H. Chen, G. Zhang, X. Fan, Y. Wang, G. Tao, D. He, J. Shi, *Applied Catalysis B: Environmental* 141–142 (2013) 42.
- [43] C.D. Wagner, L.E. Davis, M.V. Zeller, J.A. Taylor, R.H. Raymond, L.H. Gale, *Surface and Interface Analysis* 3 (1981) 211.
- [44] F. Rojas, I. Kornhauser, C. Felipe, J.M. Esparza, S. Cordero, A. Dominguez, J.L. Riccardo, *Physical Chemistry and Chemical Physics* 4 (2002) 2346.
- [45] B.C. Gagea, Y. Lorguilloux, Y. Altintas, P.A. Jacobs, J.A. Martens, *Journal of Catalysis* 265 (2009) 99.
- [46] P. Li, E.Y. Jiang, H.L. Bai, *Journal of Physics D: Applied Physics* 44 (2011) 075003.
- [47] M. Chigane, M. Ishikawa, *Journal of Electrochemical Society* 147 (2000) 2246.
- [48] M. Toupin, T. Brousse, D. Bélanger, *Chemistry of Materials* 14 (2002) 3946.
- [49] C.H. Liang, C.S. Hwang, *Journal of Alloys Compounds* 500 (2010) 102.
- [50] F. Xiao, Y. Xu, *International Journal of Electrochemical Science* 7 (2012) 7440.
- [51] H. Wang, Y. Yang, J. Xu, H. Wang, M. Ding, Y. Li, *Journal of Molecular Catalysis A: Chemical* 326 (2010) 29.
- [52] P. Prasad, J.W. Bae, K.W. Jun, K.W. Lee, *Catalysis Surveys from Asia* 12 (2008) 170.
- [53] C. Yang, H.B. Zhao, Y.L. Hou, D. Ma, *Journal of the American Chemical Society* 134 (2012) 15814.
- [54] D.J. Dwyer, J.H. Hardenbergh, *Journal of Catalysis* 87 (1984) 66.
- [55] C.S. Kuivila, J.B. Butt, P.C. Stair, *Applied Surface Science* 32 (1988) 99.
- [56] W. Wang, S. Wang, X. Ma, J. Gong, *Chemical Society Reviews* 40 (2011) 3703.
- [57] R.W. Dörner, D.R. Hardy, F.W. Williams, H.D. Willauer, *Energy and Environmental Science* 3 (2010) 884.
- [58] R.A. Dector, A.T. Bell, *Journal of Catalysis* 97 (1986) 121.
- [59] D.B. Bukur, L. Nowicki, R.K. Manne, X.S. Lang, *Journal of Catalysis* 155 (1995) 366.
- [60] S.Z. Li, W.P. Ding, G.D. Meitzner, E. Iglesia, *Journal of Physical Chemistry B* 106 (2002) 85.
- [61] H. Schulz, T. Riedel, G. Schaub, *Topics in Catalysis* 32 (2005) 117.
- [62] J.F. Bengoa, A.M. Alvarez, M.V. Cagnoli, N.G. Gallegos, S.G. Marchetti, *Applied Catalysis A: General* 325 (2007) 68.
- [63] J. Xu, C.H. Bartholomew, *Journal of Physical Chemistry B* 109 (2005) 2392.